End-wall Effects on Freely Propagating Flames in a Shock Tube

Adam J. Susa*†, Lingzhi Zheng‡, Zach D. Nygaard‡, and Ronald K. Hanson§ Stanford University, Stanford, CA, 94305

The dynamics of flame propagation at high unburned-gas temperatures are of critical importance to the performance and operability of modern engine systems but have long existed beyond the temperature regimes accessible to controlled laboratory study. The shock-tube flame speed method has been demonstrated to enable the study of premixed, freely propagating flames over a wide range of previously unachievable engine-relevant unburned-gas temperature conditions. This study reports the first systematic investigation of end-wall-induced effects on the propagation and stability of flames subject to asymmetric flow confinement in a shock tube. Through the flexibility afforded by newly available optical access, the axial position of flame ignition was varied over a range spanning from 3.3 to 15.5 cm from the driven end wall. Experiments performed under static conditions isolated the effect of asymmetric end-wall confinement and provided an opportunity to measure the flow velocity induced by the confinement effect; results show the expected functional scaling exists between flame radius, distance from the end wall, and flow velocity, but the velocity scaling deviates from that predicted. Experiments performed behind reflected shock waves are then used to probe the interplay between the confinement and gas-dynamic effects in the post-reflected-shock environment. In a break with intuition, the post-shock results show a non-monotonic relationship between position and flame stability, with one particular distance (6.4 cm) producing significantly more severe distortion than flames ignited either nearer or farther from the end wall. Finally, experiments demonstrating the generation of hemispherically expanding flames in the shock tube are reported, providing a baseline to inform the consideration of such flames as an alternative basis for flame speed measurements. The experimental measurements reported in this work provide valuable new validation targets against which detailed modeling of confinement and gas-dynamic effects can be compared, while the side-wall observations reaffirm that spherically expanding flames suitable for use in reliable laminar flame speed measurements can be generated in a post-reflected-shock environment.

I. Nomenclature

Subscripts Ccircularity diameter d 1 region-1, pre-shock driven fill conditions pixel intensity 2 region-2, post-incident-shock conditions pressure P 5 region-5, post-reflected-shock conditions radius b burned-gas S flame speed bkgd background image time flame centroid Ttemperature f flame и velocity ignition uvelocity coefficient img experiment image vertical location inscribed circle in axial location circumscribed circle flame expansion ratio ϵ r radial direction equivalence ratio shock tube t density unburned-gas u relative to end wall w

Superscripts

0 = unstretched ★ = unconfined

^{*}Corresponding author: asusa@stanford.edu

[†]Graduate Research Assistant, Department of Mechanical Engineering, AIAA student member

[‡]Graduate Research Assistant, Department of Mechanical Engineering

[§]Professor, Department of Mechanical Engineering, AIAA Fellow

II. Introduction

The performance and operability of combustion-based engines systems are governed by the dynamics of flame propagation at high unburned-gas temperature [II-3]. Nevertheless, these high-temperature conditions have long existed beyond the capability of fundamental experimental study. By utilizing flames ignited behind reflected shock waves, which act to heat fuel-oxidizer mixtures nearly instantaneously, the shock-tube flame speed method has recently been demonstrated to enable the study of premixed, freely propagating, expanding flames across the entire range of engine-relevant unburned-gas temperatures for the first time. To date, flame speed measurements have been demonstrated at unburned-gas temperatures exceeding 1,100 K [4] and at various extents of unburned-gas reaction in the negative temperature coefficient (NTC) regime of primary reference fuels [51-7], demonstrating the unique capabilities of the method to cover the entirety of the engine-relevant temperature regime.

Impulsive heating of gases by reflected shock waves in the shock-tube flame speed technique introduces unique challenges not typically encountered in more benign, static-vessel or steady-flow configurations. In the static vessels conventionally used for spherically expanding flame (SEF) experiments [8], flames are ignited in the exact center of the vessel to ensure that wall confinement effects are symmetric and balanced. In a high-aspect-ratio shock tube, flames can be centered radially, such that the radius usable for extracting flame speeds might be expected to be well approximated by the $r_{\rm f}/r_{\rm t} < 30\%$ criteria of Burke et al. [9]. However, in the axial direction, there is an inherent asymmetry between the nearby shock-tube end wall and the open tube to the side of the flame in the direction of the driver section; the implications of this asymmetry have not yet been investigated and motivate the static experiments in the present work.

Additionally, while the reflected shock nominally stagnates the gas accelerated by the incident shock wave, small residual velocities can persist in the post-reflected-shock (region-5) gas. The region-5 core-gas flow field was recently investigated using flame image velocimetry (FIV), which found that a small but measurable axial velocity in the direction of the end wall was present Π . The combination of two phenomena was proposed to account for this axial velocity, both of which are expected to scale linearly with z, from zero at the end wall (z = 0) to a magnitude on the order of 1 cm/ms at the z = 10 cm location where measurements were performed. While accurate for the prediction of region-5 velocities, the post-shock velocity model was found to be incapable of explaining the presence and magnitude of flame distortion observed at certain high-temperature shock tube conditions Π . In this work, observations of flames ignited behind reflected shocks at different axial positions are used to provide additional insights into the region-5 flow conditions and the trade-off that exists between confinement, minimized at large z_i , and post-shock nonidealities, expected to increase with z_i .

III. Methods

A. Experimental Facility

The experimental configuration employed in the present study employs the same fundamental principles of the shock-tube flame speed method as reported first by Ferris et al. [13] while making use of significantly enhanced diagnostic capability and experimental flexibility afforded by a new, highly optically accessible imaging test section shown in Fig. [1]. The new test section replaces the section beyond the gate valve of the 11.53-cm-inner-diameter constrained-reaction-volume (CRV) shock tube described by Campbell et al. [14]; features of the facility and instrumentation upstream of the gate valve remains unchanged. The new imaging test section is constructed of 6061-T6 aluminum and features a black, hard-anodized coating to minimize the occurrence of unwanted stray reflections that might otherwise interfere with imaging diagnostics. Two pairs of opposed ports are provided at each of four locations spaced 8 cm apart along the length of the test section to provide access for pressure transducers and laser-absorption diagnostics.

Inspired by, and building upon, recent successful applications of side-wall imaging to shock-tube flame experiments [4] [10-12], the new test section features large side-wall windows 18 cm long and 6.4 cm high. The windows are designed as zero-power, cemented-doublet cylindrical lenses; the internal radius conforms to that of the shock tube, thus preventing the introduction of flow disturbances, while the element thicknesses and outer radii are selected to form an aberration-corrected singlet lens. These windows are conceptually similar to the zero-power cylindrical singlet windows employed by Zabeti et al. [15], with the critical refinement that the use of a cemented doublet significantly reduces the level of cylindrical aberration compared to a singlet lens and makes the windows compatible with classical schlieren imaging [16].

Along the top and bottom of the tube, two high-aspect-ratio, 2-cm-wide slot windows provide ignition laser access over a continuous range of positions spanning from immediately adjacent to the end wall up to z = 18 cm away. These windows feature flat surfaces to minimize their effect on the focusing of the ignition laser; their width is correspondingly

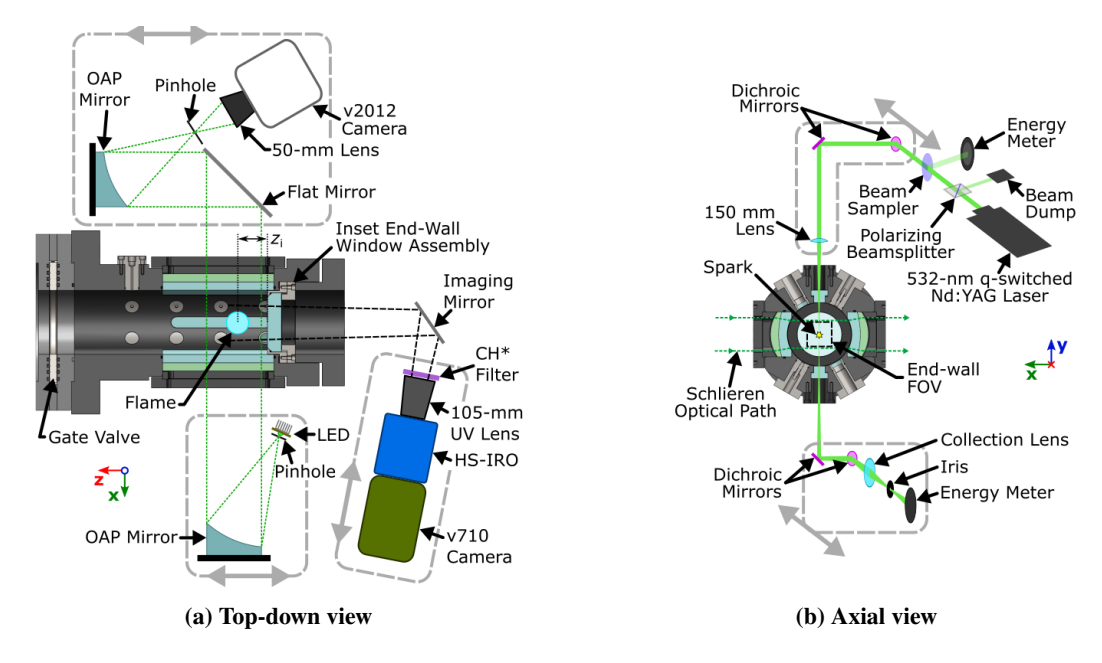


Fig. 1 Experimental configuration for flame experiments in the shock tube. Imaging instrumentation is shown in the top-down cross-sectional view (a); light-gray dashed borders outline optical sub-assemblies, which were translated in directions indicated by the associated arrows to enable imaging of different axial locations. The ignition laser optical arrangement is shown in the end-on axial cross section at the plane of the spark (b); pitch-and catch-side optical sub-assemblies were translated along the axis of the tube (in and out of the page in (b), shown as oblique angle) to vary the ignition location, z_i .

kept small to minimize the introduction of flow disturbances. These slot windows are similar in design to those used to provide side-wall emission and schlieren imaging access in several prior shock-tube studies [17-19].

Two different end-wall configurations were employed in the present study. The first, an end-wall window comprised of a simple ultraviolet- (UV-)grade quartz disk housed in a Teflon retainer, was adopted from the pioneering end-wall imaging work of Troutman et al. [20]; the use of such a window in the present work provides end-wall imaging access covering the entire radial extent of the tube but positions the end wall 2 cm outside of the side-wall field of view and was only used for experiments in which flames were ignited at $z_i > 5$ cm. The second configuration (shown in Fig. [1a]) consists of an undersized window retained in a two-piece metallic housing that allows the window to be inset 2.2 cm into the shock tube, thus positioning it 2 mm within the field of view (FOV) of the side-wall windows. A conical taper on the side of the window facing into the shock tube mates with a matching contour in the housing to retain the window when the tube is under vacuum; thin Teflon patches on the mating surface prevent metal-on-glass contact and associated stress concentrations. An O-ring in a triangular groove provides a crush seal between the glass window and housing while simultaneously helping to center the window in the housing. This configuration was used in this study for experiments with $z_i < 5$ cm.

B. Instrumentation

Flames are ignited within the shock tube by a plasma spark generated through laser-induced breakdown (LIB) (Fig. 1b). A frequency-doubled (532-nm), q-switched Nd:YAG laser (New Wave Research, Solo 120) serves as the laser source. A polarization-based variable beamsplitter allows for controlled attenuation of the 120-mJ laser pulse. The laser energy is sampled by Fresnel reflections off a flat window to measure the incident laser energy before passing through a 150-mm-focal-length lens and into the tube where LIB occurs at the beam waist radially located at the center of the tube. The portion of the beam that transmits the breakdown exits the tube through an opposing window where it is gathered by a collection lens, focused through an iris to reject emission from outside the beam path, and measured by a second energy meter. The two energy measurements allow for a differential estimation of the laser energy deposited into the spark in any given experiment, a common measurement strategy in experiments utilizing LIB [e.g., 21].

Following ignition, propagation of the flame is observed using a pair of high-speed imaging diagnostics (Fig.

Ia). As utilized in prior shock-tube flame studies, end-wall emission imaging is performed using a Phantom v710 high-speed camera coupled to a LaVision HS-IRO UV intensifier fitted with a 105-mm, f/4.5 UV-Nikkor lens. The end-wall emission camera was spectrally filtered with a 430-nm bandpass filter to selectively visualize emission from electronically excited CH* radicals concentrated within the reaction zone of the flame [22, 23]. The v710 camera records a 512- by 512-pixel sensor region at 20,000 frames per second (fps) with a 5 μs exposure time set by the intensifier.

Schlieren imaging through the side-wall windows provided for the second diagnostic. Light from a high-intensity, continuous-wave (CW) light-emitting diode (CREE XLamp XQ-E, 528 nm) passes first through a 500-µm-diameter pinhole and then through a modified Z-fold schlieren system comprised of two 4-inch-diameter, 30-degree-offset-angle off-axis parabolic (OAP) mirrors [24]. A 1-mm-diameter pinhole at the second focal point serves as the schlieren stop, producing an isotropic response of the image intensity to density gradients in all directions [25], before the transmitted light is imaged by a Phantom v2012 camera at 80,000 fps over a 384- by 512-pixel sensor region.

To facilitate varying the axial positioning of the ignition laser and imaging diagnostics, optical subsystems were assembled, indicated by the dashed-gray boarders in Fig \blacksquare that could be easily translated in the directions indicated by the corresponding arrows to reposition the ignition and imaging locations. Upon each repositioning of the imaging diagnostics, calibration images of a dot-grid target with a 5-mm pitch were recorded through both cameras. The calibration images were used to remove distortion from the images and measure the physical scaling. Schlieren images, which feature stretching in the vertical direction due to the windows, were corrected to a 52-pixel-per-cm spatial resolution, providing a roughly 8- by 5-cm FOV. Emission images, imaged through a flat end-wall window and thus exhibiting no noticeable distortion, were recorded at 88 - 100 pixels per cm depending on the particular alignment, providing a 5.1- to 5.8-cm square FOV.

C. Data Interpretation

Image and data processing is performed using the Python programming language. The "pycine" package is used for loading video sequences and associated metadata saved in Phantom's native "cine" format; Scikit-Image [26] is used for the majority of image processing tasks. Differentiation of measurements, when required, is performed using a first-derivative Savitzky-Golay type filter [27] implemented in Scipy package [28].

Quantitative measures describing the development of flames within the shock tube are extracted from side-wall schlieren image sequences. As in a prior shock-tube study employing schlieren imaging [4], background correction is performed through the conversion of schlieren image intensities to optical density (OD) on a pixel-wise basis:

$$OD = -\ln\left(\frac{I_{\text{img}}}{I_{\text{bkgd}}}\right). \tag{1}$$

The region comprising the flame is subsequently extracted from the OD images using a binarization scheme, and analyzed properties are defined with respect to these extracted binary regions. The maximum extents, d, of the flames in the Z (axial) and Y (vertical) directions are extracted and used to calculate S_b , as done in [12]:

$$S_{b,j} = \frac{\mathrm{d}r_j}{\mathrm{d}t} \quad \text{for } j \in \{z, y\},$$
 (2)

where $r_i = d_i/2$, and the aspect ratio (AR) of the flames:

$$AR_{z/y} = \frac{d_z}{d_y}. (3)$$

Circularity is calculated for each binary image as the ratio between the radii of the largest inscribed and smallest circumscribed circles centered at the flame centroid:

$$C = \frac{d_{\text{in,max}}}{d_{\text{out min}}}.$$
 (4)

Finally, the positions of the flame centroids are tracked through the video sequences, providing the basis of flame image velocimetry (FIV) [10, [11]] measurements reported for both static and shocked experiments:

$$u_j = \frac{\mathrm{d}j_c}{\mathrm{d}t} \quad \text{for } j \in \{z, y\} \,. \tag{5}$$

^{*}URL: https://github.com/ottomatic-io/pycine

Where useful for comparison to quantitative measurements, simulated results of one-dimensional laminar flame speed calculations performed in Chemkin Pro utilizing the AramcoMech 3.0 reaction mechanism are provided [29].

Emission images are presented, in the present work, for qualitative comparison to previous studies in which only emission imaging diagnostics were available. End-wall emission images additionally allow for qualitative assessment of the flame symmetry when compared to side-wall schlieren images recorded simultaneously in the present experiments. Further treatment of the end-wall images, including the extraction of quantitative morphology metrics, will be considered in a future extension to the present work.

IV. Results & Discussion

A. Static Results

Static experiments were performed at room temperature and atmospheric pressure using a stoichiometric ($\phi = 1$) mixture of propane in an oxidizer of 21% oxygen (O₂) and 79% argon (Ar). Static experiments were performed with the CRV gate valve closed to isolate the 40 cm of the shock tube nearest the end wall as a constant-volume cylindrical combustion vessel. Representative schlieren OD and CH* emission images from experiments with flames ignited at four different axial locations are shown in Fig. [2].

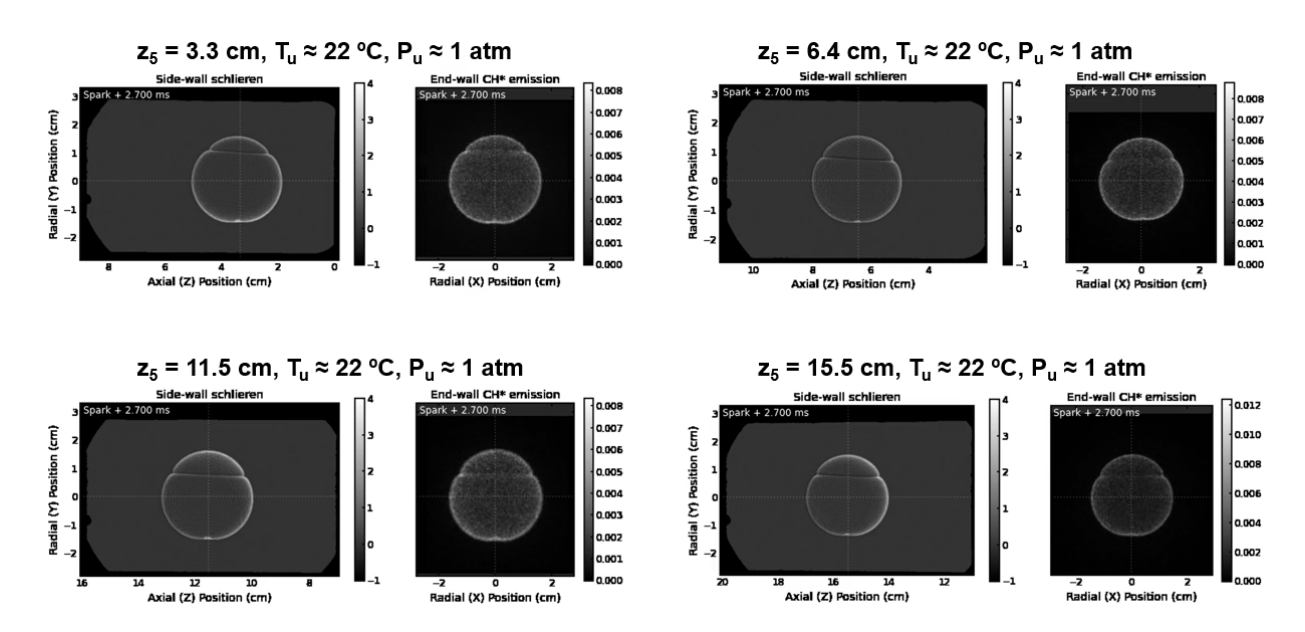


Fig. 2 Schlieren OD and CH* emission image pairs from select static experiments. Flames are shown 2.7 ms following ignition, the nominal time at which flames reach the side-wall confinement threshold. Axes show the calibrated image scale, referenced to the end wall in the Z direction and spark location in all other directions. The dotted reference lines cross at the location of ignition.

Flames are shown at a time 2.7 ms after ignition, a time at which the flames are close in size to the cylindrical side-wall confinement criteria ($r_f \approx 0.3r_w$) of Burke et al. [9]. The horizontal crease across the top half of each flame is an artifact of the third lobe of the initial LIB ignition kernel [30, 31]. Flames ignited at each location are seen to be qualitatively equivalent to one another and display substantial symmetry as viewed from the side- and end-wall orientations. The similarity is further apparent in Fig. 3 showing the measured flame speeds, which are in very close agreement between experiments after a short ignition-affected period lasting for the first 1 ms of growth. The S_b measured in the Y and Z directions agree well prior to reaching the predicted side-wall affected radius ($t \approx 2.7$ mm); at later times, cylindrical confinement leads to a plateau in $S_{b,y}$ below the value S_b^0 predicted by the Aramco 3.0 mechanism, while $S_{b,z}$ continues to increase above the predicted S_b^0 .

Aspect ratios and circularities recorded in static experiments are displayed in Fig. 4. Aspect ratios show significant variability at the earliest times but quickly converge towards unity in all cases; at the latest times, $AR_{z/y}$ increases

slightly under the effects of confinement by the cylindrical side-walls. The circularity, which is ≤ 1 by definition, monotonically increases from an initial low value when the flames are most affected by the spark to a final value > 0.9 for all flames. Both of these measures reflect the qualitative observations from Fig. 2 that static flames are symmetric and substantially spherical.

Figure 5 displays the centroid displacements and corresponding FIV measurements extracted from static experiments with flames ignited at different locations (indicated by color in the legend). Flames ignited at all positions are found to be initially stationary, as expected in a quiescent environment, before beginning to translate in the +Z direction (away from the end wall) with a velocity that increases through time. Those flames ignited nearer to the end wall tend to display larger axial displacements and velocities than those ignited farther away. Duplicated experiments with ignition at the 4.4- and 15.5-cm positions demonstrate the repeatability of the centroid position measurement results under static conditions.

In the simple model of an unconfined, spherically expanding flame, the burned gas within the flame is stagnant $(u_r^* = 0)$ and the unburned gas is pushed away from the growing flame with a velocity that falls off with the radial distance r from the centroid of the flame (Fig. 6a):

$$u_{\mathbf{r}}^{\star} = \begin{cases} 0 & r \leq r_{f^{-}} \\ -S_{\mathbf{b}} \left(\frac{\epsilon - 1}{\epsilon}\right) \left(\frac{r_{\mathbf{f}}}{r}\right)^{2} & r \geq r_{f^{+}} \end{cases}$$
 (6)

where $\epsilon = \rho_u/\rho_b$. In the simplest treatment for confinement of a flame propagating in proximity to a wall (Fig. 6b), the zero-velocity boundary condition imposed by the wall might be assumed to be maintained by the superposition of a uniform velocity field of the necessary magnitude to counteract the flame-induced velocity at the end wall predicted from the flame model:

$$u_{\rm r}(r) = u_{\rm r}^{\star}(r) - u_{\rm r}^{\star}(r = z_{\rm c}).$$
 (7)

As the constant-offset confinement model predicts a non-zero velocity in the burned gas, such a confinement effect would be apparent in the axial FIV measurements. Applied to the centroid, $u_r^*(r=0)$ equals zero and drops out of Eqn. [7] leaving:

$$u_{\rm c,z} = S_{\rm b} \left(\frac{\epsilon - 1}{\epsilon}\right) \left(\frac{r_{\rm f}}{z_{\rm c}}\right)^2 = \mathcal{U}_{\rm c,z} \left(\frac{r_{\rm f}}{z_{\rm c}}\right)^2.$$
 (8)

This expression would predict a proportional relationship between $u_{c,z}$ and $\left(\frac{r_f}{z_c}\right)^2$, an expectation borne out in Fig. 7 which shows the FIV data from the static experiments plotted on the appropriate axes along with corresponding linear fits (dashed lines). While the corresponding value of $\mathcal{U}_{c,z}$, found as the slope of the linear fits, agrees well with the quantitative prediction of 6.0 m/s expected from Eqn. 7 and calculated with results modeled using AramcoMech 3.0 for the 3.3-cm ignition case, values of $\mathcal{U}_{c,z}$ at more distant locations are larger than predicted.

The discrepancy between the constant value $\mathcal{U}_{c,z}$ predicted by the simple model and roughly proportional relationship seen between $\mathcal{U}_{c,z}$ and z_i seen in Fig. 7b is likely the result of higher-dimensional effects not accounted for in the one-dimensional confinement model. Higher dimensional flow modeling, for example using a flamelet formulation of the type employed by Burke et al. 9, would be expected to more robustly predict the magnitude of the confinement-induced velocity and is a topic of ongoing study. The experimental data reported here will provide valuable benchmarks against which the output of such models will be validated to confirm their predictiveness and accuracy.

B. Post-Reflected-Shock Results

Using the same $\phi = 1$ propane/O₂/Ar mixture and ignition locations, experiments were additionally performed with flames ignited behind reflected shocks at elevated temperatures near 650 K (644 K $\leq T_5 \leq$ 667 K) and atmospheric pressure (0.99 atm $\leq P_5 \leq$ 1.06 atm). A driver-gas mixture of 60% nitrogen and 40% helium was selected to provide the desired shock strength at a driver pressure accessible with a single polycarbonate diaphragm. A driver insert [32], designed using the 1-D StanShock code [33], was used to minimize post-shock pressure change at the target condition, providing near-constant-pressure test times exceeding 5 ms in the absence of a flame.

In reflected-shock experiments, the ignition laser and camera recordings were triggered relative to the reflected shock passing a PCB pressure transducer near the ignition location. Short spark-delay times of $290 - 540 \,\mu s$ relative to the reflected shock passing the ignition location were used in post-shock experiments, with the variation being the result of the relative positioning of the trigger PCB and ignition location. The positions of the incident and reflected shocks in

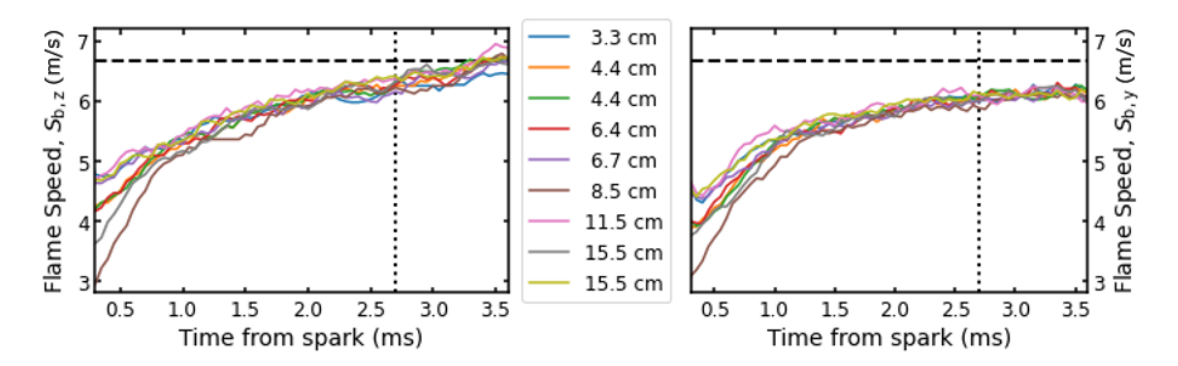


Fig. 3 Propagation speed measured in the axial (left) and vertical (right) directions as functions of time for flames ignited at different axial positions in static, room-temperature experiments. Vertical dotted line indicates the approximate time the flame exceeds the nominal 30% side-wall confinement threshold. Dashed horizontal line represents the modeled unstretched, burned flame speed calculated at 650 K using AramcoMech 3.0.

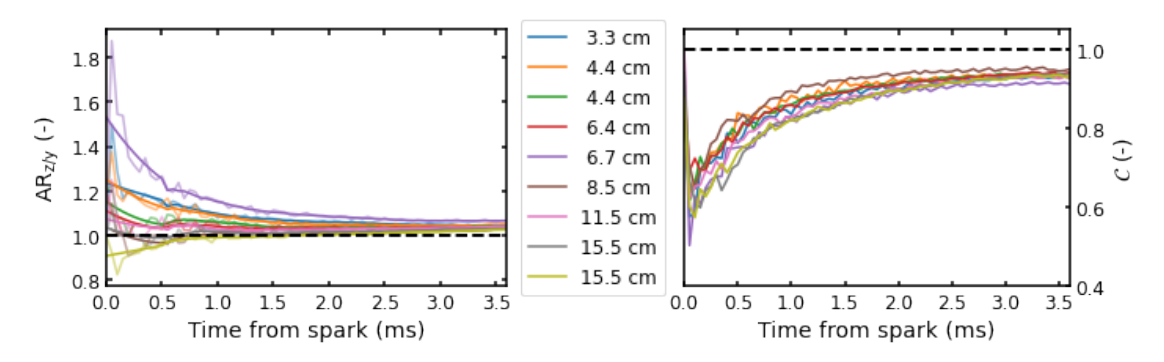


Fig. 4 Aspect ratio (left) and circularity (right) as functions of time for flames ignited at different axial positions in static, room-temperature experiments.

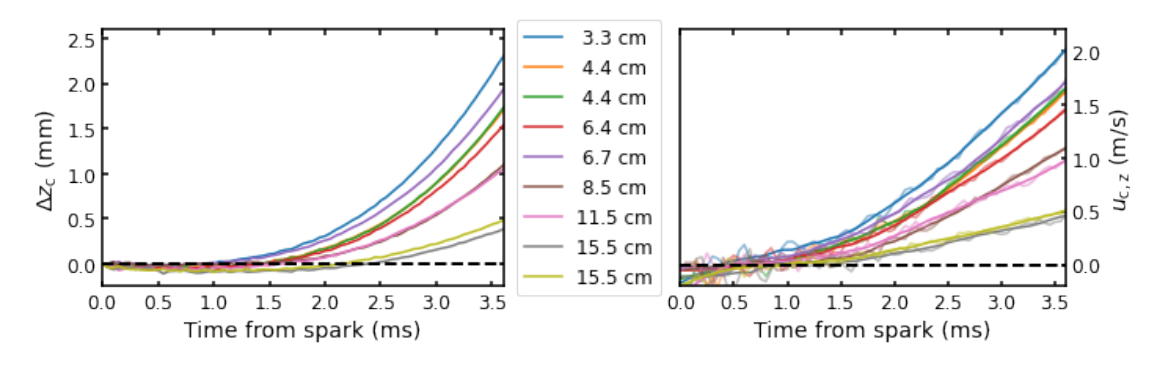


Fig. 5 Axial displacements (left) and velocities (right) of flames ignited at different axial positions in static, room-temperature experiments.

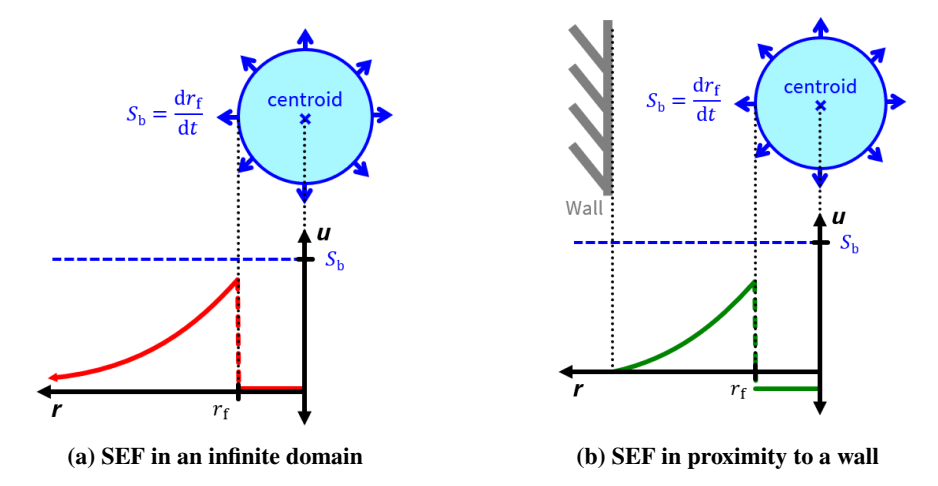


Fig. 6 Schematics of gas velocities associated with the simple model of a spherically expanding flame (SEF) with and without the presence of a confining wall.

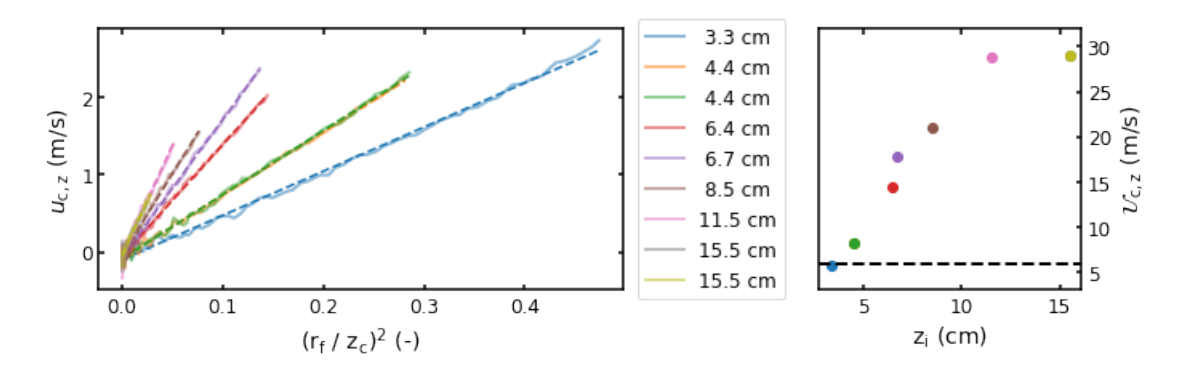


Fig. 7 Linearized centroid velocity data and fits (left) and slopes of the fits (right). The dashed line in the right plot indicates the analytical value of $\mathcal{U}_{c,z}$ obtained from modeled results using the AramcoMech 3.0 mechanism. While the absolute magnitude of the axial velocity tends to decreases with z_i , the velocity coefficients $\mathcal{U}_{c,z}$ increase steadily with z_i to values much larger than that predicted by the simple confinement model.

schlieren recordings provide the required information to determine both the precise ignition time relative to the reflected shock and the position of the schlieren FOV relative to the driven end wall.

Image pairs showing flames ignited behind reflected shocks at six different distances from the end wall are presented in Fig. 8. All flames are shown 1.5 ms after ignition, a time where the flame radius is near the side-wall confinement threshold. Unlike in a static environment, where flames showed little, if any, qualitative difference between ignition locations, greater morphological variability is observable in the post-reflected-shock flame experiments.

The majority of the flames appear nominally circular in both the schlieren and emission images, suggesting an overall spherical morphology consistent with the necessary condition for use in a laminar flame speed measurement. Figure \mathcal{P} shows the flame propagation speeds in the axial and vertical directions (left and right plots, respectively) as obtained from the schlieren recordings using Eqn. \mathcal{P} . Setting aside, for a moment, the measurements corresponding to the $z_i = 3.3$ -cm (blue) and 6.4-cm (green) flames, extracted value of S_b are seen to be in close agreement (within 10%) both between experiments and across orientations until the flames reach the critical confinement radius at a time near 1.5 ms. This observation suggests that flames ignited at any of the locations $z_i = \{4.4, 8.5, 11.5, 15.5\}$ cm could reasonably be used as the basis of a reliable, high-temperature laminar flame speed measurement.

Looking now to the outlying cases, distortion occurred to a significant extent in the flame ignited 6.4 cm from the end wall and to a lesser degree in the flame at 3.3 cm. The axial distortion of the 6.4-cm flame seen from the side wall notably resembles that reported in a recent side-wall emission imaging study [12]. This axial distortion corresponds to the concentric rings visible in the end-wall emission image of the same experiment, an image artifact identified in earlier

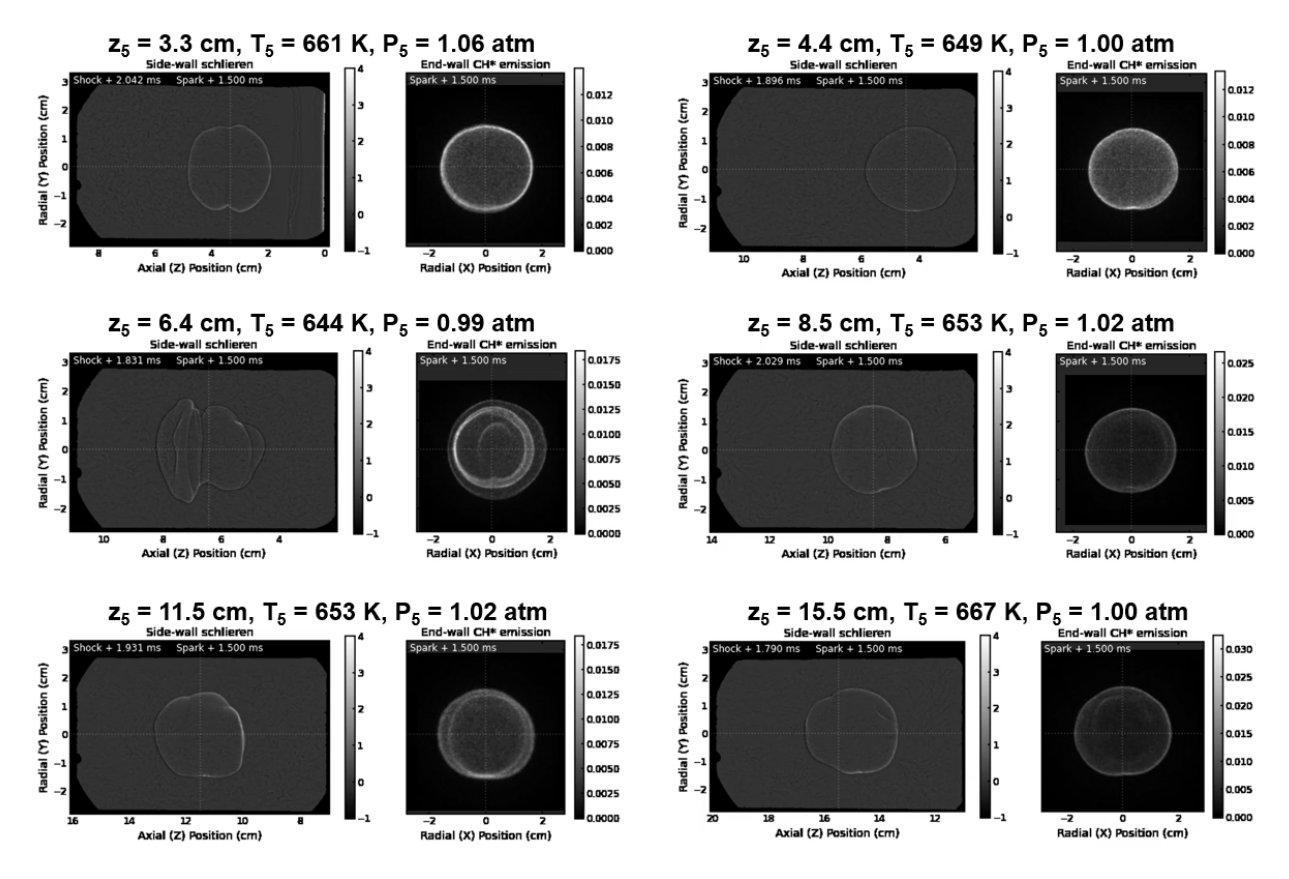


Fig. 8 Schlieren OD and CH* emission image pairs from each post-reflected-shock experiment. Flames are shown 1.5 ms following ignition, the nominal time at which flames reach the side-wall confinement threshold. Axes show the calibrated image scale, referenced to the end wall in the Z direction and spark location in all other directions. The dotted reference lines cross at the location of ignition.

shock-tube flame studies [G, T]. The effect of the distortion on the apparent propagation rate is readily ascertained from Fig. [G, T], where the flame ignited at 6.4 cm displays the largest measured S_b in both the Z and Y directions. This result is attributed to an enhanced overall burning rate due to the increased flame-front area of the distorted flame as compared to the ideal spherical morphology.

The 3.3-cm flame also shows some degree of distortion in the images and produces S_b values that deviate somewhat from the majority of other experiments reported in Fig. [9], with its value $S_{b,z}$ being somewhat low and $S_{b,y}$ appearing higher than most. Unlike the uniformly elevated propagation rates associated with the increased burning area of the 6.4-cm flame, however, these results would substantially offset each other when averaged across the Y and Z directions, providing a value in reasonable agreement with the other experiments. This would suggest that, while the 3.3-cm flame was subjected to axial compression and radial stretching of the type discussed in [12], it otherwise propagates in a steady, laminar manner. While side-wall imaging of such a flame could, therefore, reasonably be used to provide a laminar flame speed measurement, the radial stretching would lead to an incorrect value if a burning velocity was extracted from end-wall images alone.

Figure $\boxed{10}$ contains the aspect ratio and circularity measures of the post-reflected-shock flames. Aspect ratios begin well above one but rapidly approach unity during the first 0.6 ms of growth for all but the distorted, 6.4-cm flame that does not approach unity AR until later times. As a measure of experimental quality, C (Fig. $\boxed{10}$, right) more clearly differentiates the distorted, 6.4-cm flame from the more ideal flames ignited at other axial locations than AR. While all flames begin with $C \approx 0.5$, the 6.4-cm flame is alone remaining below 0.6 during the entire measurement period, with C increasing to above 0.8 for all other flames. In the cases of the flames ignited at 4.4 and 8.5 cm, the circularity reaches a value as high as 0.9, a value approaching that seen under fully quiescent conditions in the static experiments (Fig. $\boxed{4}$). The finding that flame circularities comparable to static experiments can be achieved in the post-shock environment

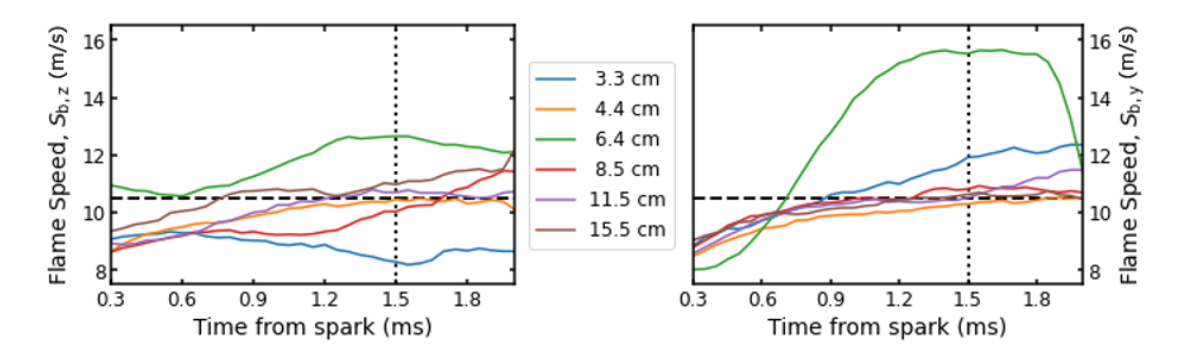


Fig. 9 Propagation speed measured in the axial (left) and vertical (right) directions as functions of time for flames ignited at different axial positions in elevated-temperature, post-reflected-shock experiments. Vertical dotted line indicates the approximate time the flame exceeds the nominal 30% side-wall confinement threshold. Dashed horizontal line represents the modeled unstretched, burned flame speed at $T_{\rm u} = 650~{\rm K}$ modeled using the AramcoMech 3.0 kinetic mechanism.

supports the notion that nearly spherical, laminar flames can be generated at high temperature within a shock tube as are required for accurate and reliable flame speed measurements. As all flames ignited at locations other than 6.4 cm show reasonable agreement in Z-Y averaged S_b values both with one another and the S_b^0 predicted by AramcoMech 3.0, these measurements suggest that C is preferable to AR for the characterization of flame morphology with respect to use in flame speed measurements for its ability to clearly differentiate flames based on the degree of distortion.

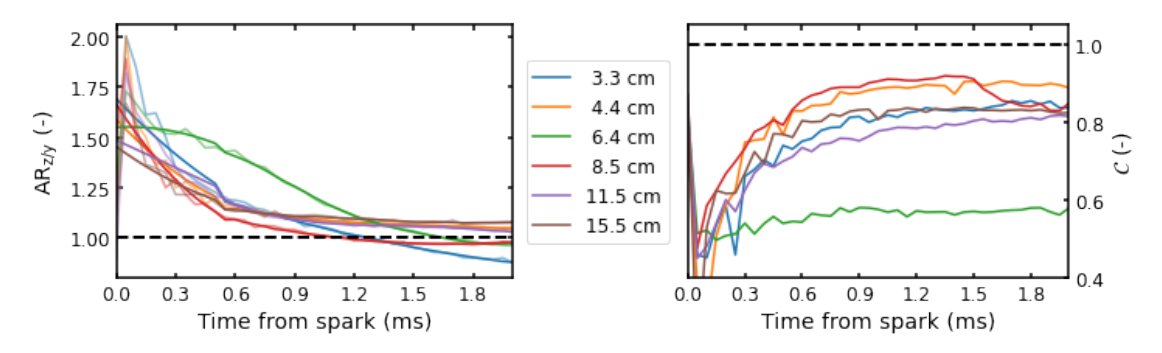


Fig. 10 Aspect ratio (left) and circularity (right) as functions of time for flames ignited at different axial positions in elevated-temperature, post-reflected-shock experiments.

Finally, centroid axial displacements and FIV-measured velocities are shown for reflected-shock experiments in Fig. The centroid velocities at t = 0, which are expected to reflect the velocity of the underlying region-5 flow-field, do not strictly follow the predicted direct dependence with the axial position [10, 11]. The flame ignited at 15.5 cm, the largest z_i , displays both the largest initial velocity and overall displacement, consistent with the expectation of increasing nonidealities in the gas located further from the end wall. The flames ignited nearer the end wall, however, show somewhat less predictable axial motions. As with the FIV measurements from static experiments, the post-shock FIV data provide valuable benchmarks against which the predictions of future efforts to model coupled confinement and post-shock gas-dynamic effects can be evaluated. In addition, the finding that no clear correlation exists between the centroid velocity and subsequent flame stability provides the useful practical insight that the phenomenon responsible for undesirable flame distortion may be unrelated to the small bulk velocity now understood to exist in the region-5 environment.

C. Hemispherically Expanding Flame Demonstration

A final pair of experiments is presented providing a first demonstration of end-wall bounded, hemispherically expanding flames ignited in static and post-reflected-shock environments. Figure 12 presents a schematic of a hemispherical flame, which is initiated within the imaging test section by angling the ignition laser such that the beam

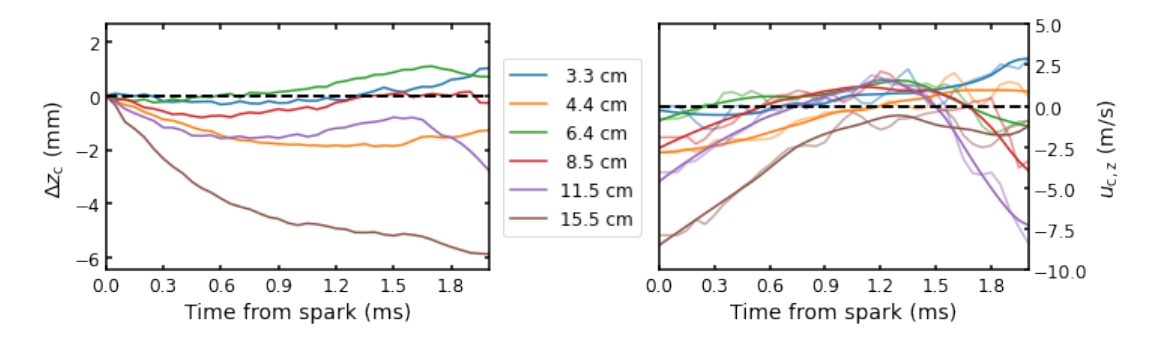


Fig. 11 Axial displacements (left) and velocities (right) of flames ignited at different axial positions in elevated-temperature, post-reflected-shock experiments.

waist impinges on the surface of an aluminum end wall. The metallic end wall features the same top-hat profile as the inset end-wall window assembly, such that the end-wall surface falls within the view of the side-wall schlieren images. As the end-wall window is not used in these experiments, emission images were not recorded.

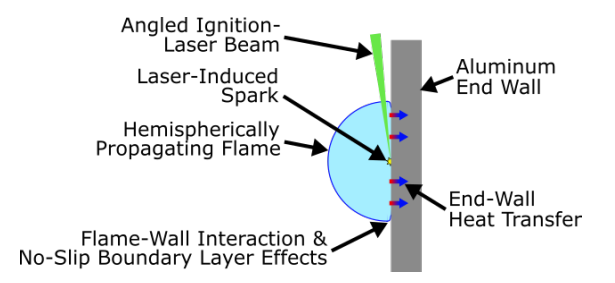


Fig. 12 Schematic of an end-wall bounded hemispherical flame ignited by directing the focused ignition laser beam onto the surface of an aluminum end wall. While a hemispherical flame of this type is not be subjected to confinement effects, it is impacted by heat transfer, the no-slip boundary layer, and flame-wall interactions.

The motivation for exploring the use of hemispherically expanding flames is that the end wall naturally imposes the zero-axial-velocity condition that exists along the center line of an ideal spherically expanding flame. In a post-shock environment, where non-idealities are present that may introduce undesirable motion into the region-5 gas, the enforcement such a boundary condition could provide a means to help counteract the non-ideal effects. However, the end-wall-imposed boundary condition also carries its own potential liabilities, as heat transfer to the end wall, the no-slip boundary condition along the surface of the end wall, and flame-wall interactions could all affect the dynamics of the flame. The relative utility of such flames should therefore be assessed by considering the magnitudes of each relevant effect and the extent to which they can be accounted for or mitigated.

Sample images of the hemispherically expanding flames ignited in this manner are presented in Fig. [13]. In both static and post-shock environments, the flames are both observed to be relatively smooth, providing initial promise for their potential use as a basis for laminar flame speed measurements. Measured propagation speeds, shown in Fig. [14] show close agreement between the two orientations in the static case; a more significant discrepancy exists in the high-temperature experiment. Furthermore, in both cases, the flame speed in the axial (Z) direction increases steadily as time progresses, whereas the radial (Y) velocities remain more constant. This suggests the flow fields induced by hemispherical flames might be more universal across experimental conditions than for unbounded, spherically expanding flames. The modeling of such flames could provide further insight into the dynamics of hemispherical flames; the present data will provide valuable experimental comparisons for validating any such models.

V. Conclusion

Results of the first systematic, comparative study of the end-wall confinement and axial positioning effects on freely propagating flames in a shock tube environment have been reported. Novel experimental capabilities provided significantly enhanced optical access and flexibility in the configuration of shock-tube flame speed experiments. In static

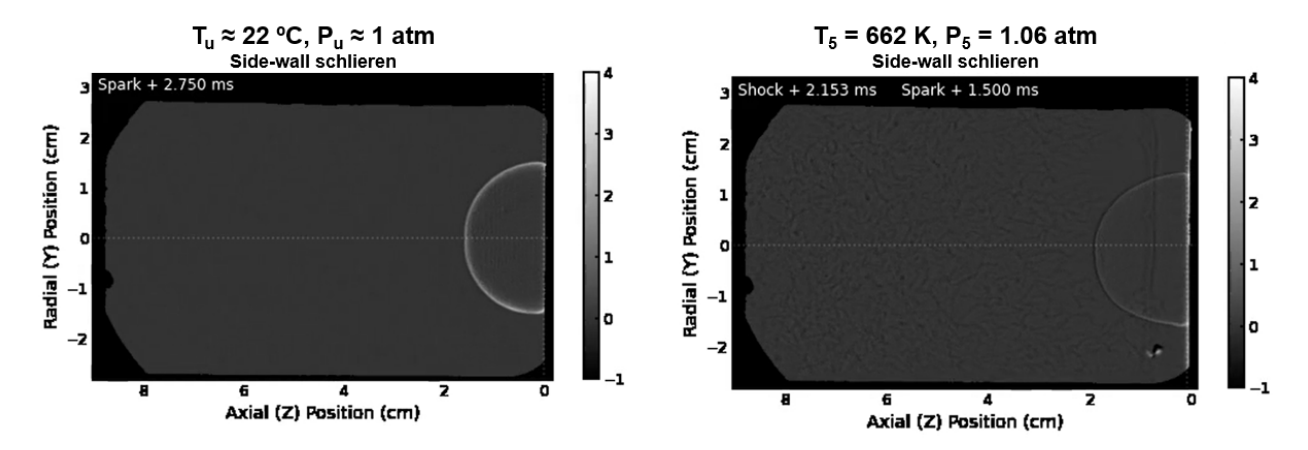


Fig. 13 Images of hemispherical flames ignited in static (left) and post-reflected-shock (right) environments. Under both sets of conditions, flames are observed to be qualitatively smooth but exhibit some difference in their shapes.

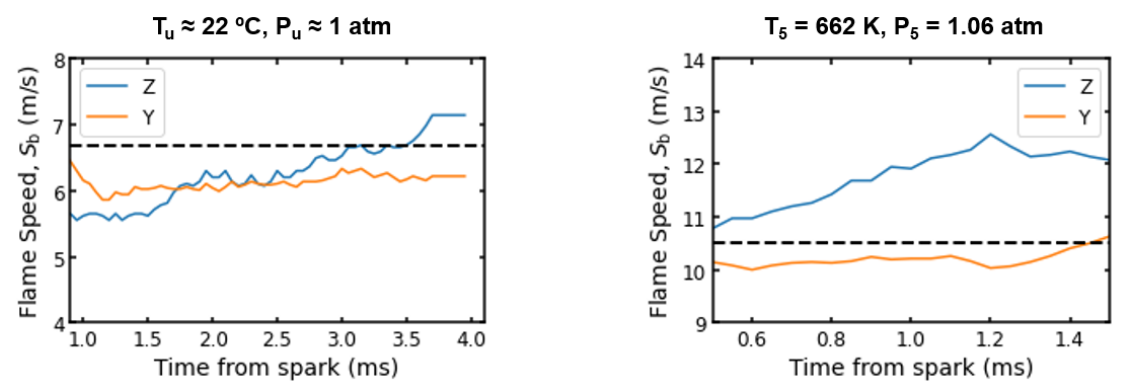


Fig. 14 Burned flame speed measurements extracted from the flame ignited in a static (left) and post-shock (right) environment. In both cases, the propagation speed in the axial direction increases steadily through time, while the speed in the radial direction remains nearly constant. Propagation speeds at both conditions show reasonable agreement with the 1-D burned flame speed modeled with AramcoMech 3.0 (dashed lines).

experiments, substantially spherical flames producing consistent S_b measurements were observed at ignition locations from 3.3-15.5 cm from the end wall. The displacement of the flames as a result of asymmetric confinement by the end wall was found to display the functional scaling predicted by a simple, one-dimensional confinement model. While the simple model was not able to reliably predict the velocity magnitude due to its exclusion of higher-dimensional flow effects, measurements reported in this work will provide critical experimental targets against which future confinement models can be validated.

Flames ignited at various distances from the end wall behind reflected shocks at temperatures near 650 K validated that nearly spherical, laminar flames can be generated in a post-shock environment and provided new data in support of efforts to understand the conditions under which flames become subjected to distortion and instability. Flames ignited at four locations, $z_i = \{4.4, 8.5, 11.5, 15.5\}$ cm, exhibited substantially spherical morphologies and produced consistent S_b measurements. With ignition at two other locations, $z_i = \{3.3, 6.4\}$ cm, flames were observed to exhibit varying levels of distortion with implications on the accuracy and reliability of extracted S_b values. While further study with the goal of understanding, predicting, and avoiding flame distortion of the type seen at 6.4 cm is ongoing, the application of side-wall imaging now allows for flame distortion to be unambiguously identified when present in a shock-tube experiment.

Finally, a preliminary demonstration of hemispherically expanding flames ignited against the end wall of the shock tube was reported. Qualitatively assessment of the hemispherical flames finds them to be nominally smooth and laminar in both static and post-reflected-shock environments. Quantitative flame speed measurements found the flames exhibit

somewhat different behaviors in the axial and radial directions. The application of modeling to understand both the flame-induced flow field and the impacts of other non-ideal effects (heat transfer and no-slip boundary conditions) is identified as a future direction of study to elucidate the utility of using such flames in future flame speed measurement studies.

This study demonstrates the significant benefit brought about by the application of side-wall schlieren imaging to shock-tube flame experiments. Schlieren imaging enables detailed characterization and verification of the morphology of flames, provides enhanced fidelity in the extraction of flame fronts and determination of flame speeds, and opens the door to numerous new opportunities for the detailed study of the region-5 environment. Through the improved characterization of flame morphology and the exclusion of distorted flames, future laminar flame speed measurements performed in the shock-tube will be made more accurate and reliable as a result of the side-wall imaging capability and the findings of the present investigation.

Acknowledgments

This work was supported by the U.S. National Science Foundation under award number 1940865, contract monitor Dr. John Daily. Funding support for instrumentation used in this work was provided by the U.S. Army Research Office and the U.S. Office of Scientific Research. A. J. Susa thanks the U.S. Department of Defense and Army Research Office for support under the NDSEG fellowship program.

References

- [1] Kaiser, E., Yang, J., Culp, T., Xu, N., and Maricq, M., "Homogeneous charge compression ignition engine-out emission-does flame propagation occur in homogeneous charge compression ignition?" *International Journal of Engine Research*, Vol. 3, No. 4, 2002, pp. 185–195. https://doi.org/10.1243/146808702762230897
- [2] Juneja, H., LaPointe, L. A., Ntone, F., Lyford-Pike, E. J., and Qin, X., "Development and Application of Advanced Combustion Modeling Tools for Heavy Duty Gaseous Fueled Industrial Spark Ignition Engines," *Internal Combustion Engine Division Fall Technical Conference*, Vol. 49446, 2010, pp. 741–751. https://doi.org/10.1115/ICEF2010-35061.
- [3] Puduppakkam, K. V., Modak, A. U., Wang, C., Hodgson, D., Naik, C. V., and Meeks, E., "Generating Laminar Flame Speed Libraries for Autoignition Conditions," *Turbo Expo: Power for Land, Sea, and Air*, Vol. 84133, American Society of Mechanical Engineers, 2020, p. V04BT04A004. https://doi.org/10.1115/GT2020-15274.
- [4] Susa, A. J., Zheng, L., and Hanson, R. K., "Schlieren-based measurements of propane flame speeds at extreme temperatures," 12th US National Combustion Meeting, 2021, p. 1G05. URL https://www.researchgate.net/publication/351735317_Schlieren-based measurements of propane flame speeds at extreme temperatures.
- [5] Susa, A. J., Ferris, A. M., Davidson, D. F., and Hanson, R. K., "Experimental Shock Tube Measurements of Laminar Burning Velocity of n-Heptane and iso-Octane in the Negative Temperature Coefficient Regime," *AIAA Scitech 2019 Forum*, 2019, p. 0460. https://doi.org/10.2514/6.2019-0460.
- [6] Susa, A. J., Ferris, A. M., Davidson, D. F., and Hanson, R. K., "Experimental observation of negative temperature dependence in iso-octane burning velocities," *AIAA Journal*, Vol. 57, No. 10, 2019, pp. 4476–4481. https://doi.org/10.2514/1.J058530.
- [7] Susa, A., Ferris, A., Davidson, D., and Hanson, R., "Experimental measurement of laminar burning velocity of *n*-heptane at variable extents of reaction in a shock tube," *Proc. of the 32nd International Symposium on Shock Waves (ISSW32)*, 2019, p. 0149. https://doi.org/10.3850/978-981-11-2730-4_0149-cd.
- [8] Egolfopoulos, F., Hansen, N., Ju, Y., Kohse-Höinghaus, K., Law, C., and Qi, F., "Advances and challenges in laminar flame experiments and implications for combustion chemistry," *Progress in Energy and Combustion Science*, Vol. 43, 2014, pp. 36–67. https://doi.org/10.1016/j.pecs.2014.04.004.
- [9] Burke, M. P., Chen, Z., Ju, Y., and Dryer, F. L., "Effect of cylindrical confinement on the determination of laminar flame speeds using outwardly propagating flames," *Combustion and Flame*, Vol. 156, No. 4, 2009, pp. 771–779. https://doi.org/10.1016/j.combustflame.2009.01.013.
- [10] Susa, A. J., and Hanson, R. K., "Flame-drift velocimetry and flame morphology measurements with dual-perspective imaging in a shock tube," 12th US National Combustion Meeting, 2021, p. 1G13. URL https://www.researchgate.net/publication/351735109_Flame-drift_velocimetry_and_flame_morphology_measurements_with_dual-perspective_imaging_in_a_shock_tube.

- [11] Susa, A. J., and Hanson, R. K., "Flame image velocimetry: Seedless characterization of post-reflected-shock velocities in a shock-tube," *Experiments in Fluids*, In Review.
- [12] Susa, A. J., and Hanson, R. K., "Distortion of expanding n-heptane flames at high unburned-gas temperatures behind reflected shocks," *Combustion and Flame*, Vol. 237, 2022, p. 111842. https://doi.org/10.1016/j.combustflame.2021.111842.
- [13] Ferris, A. M., Susa, A. J., Davidson, D. F., and Hanson, R. K., "High-temperature laminar flame speed measurements in a shock tube," *Combustion and Flame*, Vol. 205, 2019, pp. 241–252. https://doi.org/10.1016/j.combustflame.2019.04.007.
- [14] Campbell, M. F., Tulgestke, A. M., Davidson, D. F., and Hanson, R. K., "A second-generation constrained reaction volume shock tube," *Review of Scientific Instruments*, Vol. 85, No. 5, 2014, p. 055108. https://doi.org/10.1063/1.4875056.
- [15] Zabeti, S., Fikri, M., and Schulz, C., "Reaction-time-resolved measurements of laser-induced fluorescence in a shock tube with a single laser pulse," *Review of Scientific Instruments*, Vol. 88, No. 11, 2017, p. 115105. https://doi.org/10.1063/1.5010228.
- [16] Susa, A., and Hanson, R., "Optical design of afocal windows for curved-wall vessels," Applied Optics, In Preparation.
- [17] Wang, B., Olivier, H., and Grönig, H., "Ignition of shock-heated H2-air-steam mixtures," *Combustion and flame*, Vol. 133, No. 1-2, 2003, pp. 93–106. https://doi.org/10.1016/S0010-2180(02)00552-7.
- [18] Lee, C., Vranckx, S., Heufer, K. A., Khomik, S. V., Uygun, Y., Olivier, H., and Fernandez, R. X., "On the chemical kinetics of ethanol oxidation: shock tube, rapid compression machine and detailed modeling study," *Zeitschrift für Physikalische Chemie*, Vol. 226, No. 1, 2012, pp. 1–28. https://doi.org/10.1524/zpch.2012.0185
- [19] Figueroa-Labastida, M., and Farooq, A., "Simultaneous lateral and endwall high-speed visualization of ignition in a circular shock tube," *Combustion and Flame*, Vol. 214, 2020, pp. 263–265. https://doi.org/10.1016/j.combustflame.2019.12.033.
- [20] Troutman, V. A., Strand, C. L., Campbell, M. F., Tulgestke, A. M., Miller, V. A., Davidson, D. F., and Hanson, R. K., "High-speed OH* chemiluminescence imaging of ignition through a shock tube end-wall," *Applied Physics B*, Vol. 122, No. 3, 2016, p. 56. https://doi.org/10.1007/s00340-016-6326-y.
- [21] Syage, J., Fournier, E., Rianda, R., and Cohen, R., "Dynamics of flame propagation using laser-induced spark initiation: Ignition energy measurements," *Journal of Applied Physics*, Vol. 64, No. 3, 1988, pp. 1499–1507. https://doi.org/10.1063/1.341824.
- [22] Kauranen, P., Andersson-Engels, S., and Svanberg, S., "Spatial mapping of flame radical emission using a spectroscopic multi-colour imaging system," *Applied Physics B*, Vol. 53, No. 4, 1991, pp. 260–264. https://doi.org/10.1007/BF00357147.
- [23] Alviso, D., Mendieta, M., Molina, J., and Rolón, J. C., "Flame imaging reconstruction method using high resolution spectral data of OH*, CH* and C2* radicals," *International Journal of Thermal Sciences*, Vol. 121, 2017, pp. 228–236. https://doi.org/10.1016/j.ijthermalsci.2017.07.019.
- [24] Zheng, L., Susa, A., and Hanson, R., "Compact schlieren system design using planar geometric ray tracing," *Applied Optics*, In Preparation.
- [25] Settles, G. S., Schlieren and shadowgraph techniques: visualizing phenomena in transparent media, Springer Science & Business Media, 2001, Chap. 5 Specialized schlieren techniques, pp. 116–118.
- [26] van der Walt, S., Schönberger, J. L., Nunez-Iglesias, J., Boulogne, F., Warner, J. D., Yager, N., Gouillart, E., Yu, T., and the scikit-image contributors, "scikit-image: image processing in Python," *PeerJ*, Vol. 2, 2014, p. e453. https://doi.org/10.7717/peerj.453.
- [27] Savitzky, A., and Golay, M. J., "Smoothing and differentiation of data by simplified least squares procedures." *Analytical chemistry*, Vol. 36, No. 8, 1964, pp. 1627–1639. https://doi.org/10.1021/ac60214a047.
- [28] Virtanen, P., and et al., "SciPy 1.0: Fundamental Algorithms for Scientific Computing in Python," *Nature Methods*, Vol. 17, 2020, pp. 261–272. https://doi.org/10.1038/s41592-019-0686-2.
- [29] Zhou, C.-W., Li, Y., Burke, U., Banyon, C., Somers, K. P., Ding, S., Khan, S., Hargis, J. W., Sikes, T., Mathieu, O., et al., "An experimental and chemical kinetic modeling study of 1, 3-butadiene combustion: Ignition delay time and laminar flame speed measurements," *Combustion and Flame*, Vol. 197, 2018, pp. 423–438. https://doi.org/10.1016/j.combustflame.2019.10.015
- [30] Bradley, D., Sheppard, C., Suardjaja, I., and Woolley, R., "Fundamentals of high-energy spark ignition with lasers," *Combustion and Flame*, Vol. 138, No. 1-2, 2004, pp. 55–77. https://doi.org/10.1016/j.combustflame.2004.04.002
- [31] Dumitrache, C., and Yalin, A. P., "Gas dynamics and vorticity generation in laser-induced breakdown of air," *Optics express*, Vol. 28, No. 4, 2020, pp. 5835–5850. https://doi.org/10.1364/OE.385430.

- [32] Hong, Z., Pang, G. A., Vasu, S. S., Davidson, D. F., and Hanson, R. K., "The use of driver inserts to reduce non-ideal pressure variations behind reflected shock waves," *Shock Waves*, Vol. 19, No. 2, 2009, pp. 113–123. https://doi.org/10.1007/s00193-009-0205-y.
- [33] Grogan, K., and Ihme, M., "Stanshock: A gas-dynamic model for shock tube simulations with non-ideal effects and chemical kinetics," *Shock Waves*, Vol. 30, No. 4, 2020, pp. 425–438. https://doi.org/10.1007/s00193-019-00935-x